

A Tale of Two Tails: Exploring Stellar Populations in the Tidal Tails of NGC 3256

Michael Rodruck,^{1*} Iraklis Konstantopoulos,² Karen Knierman,^{3,4} Konstantin Fedotov,^{5,6}
 Brendan Mullan,^{7,8} Sarah Gallagher,⁵ Patrick Durrell,⁹ Robin Ciardullo,^{1,10}
 Caryl Gronwall,^{1,10} and Jane Charlton¹

¹*Department of Astronomy and Astrophysics, The Pennsylvania State University, University Park, PA 16802, USA*

²*Australian Astronomical Observatory, North Ryde, NSW 2133, Australia*

³*School of Earth & Space Exploration, Arizona State University, 550 E. Tyler Mall, Room PSF-686 (P.O. Box 871404), Tempe, AZ 85287-1404, USA*

⁴*NSF Astronomy and Astrophysics Postdoctoral Fellow*

⁵*University of Western Ontario, London, ON N6A 3K7, Canada*

⁶*Herzberg Institute of Astrophysics, National Research Council of Canada, Victoria, BC V9E 2E7, Canada*

⁷*Point Park University Natural Sciences and Engineering Department 201 Wood St Pittsburgh PA 15222, USA*

⁸*Blue Marble Space Institute of Science 1001 4th Ave, Suite 3201 Seattle, WA 98154, USA*

⁹*Department of Physics and Astronomy, Youngstown State University, Youngstown, OH 44555, USA*

¹⁰*Institute for Gravitation and the Cosmos, The Pennsylvania State University, University Park, PA 16802, USA*

Accepted XXX. Received YYY; in original form ZZZ

ABSTRACT

We have developed an observing program using deep, multiband imaging to probe the chaotic regions of tidal tails in search of an underlying stellar population, using NGC 3256’s 400 Myr twin tidal tails as a case study. These tails have different colours of $u - g = 1.05 \pm 0.07$ and $r - i = 0.13 \pm 0.07$ for NGC 3256W, and $u - g = 1.26 \pm 0.07$ and $r - i = 0.26 \pm 0.07$ for NGC 3256E, indicating different stellar populations. These colours correspond to simple stellar population ages of 288^{+11}_{-54} Myr and 841^{+125}_{-157} Myr for NGC 3256W and NGC 3256E, respectively, suggesting NGC 3256W’s diffuse light is dominated by stars formed after the interaction, while light in NGC 3256E is primarily from stars that originated in the host galaxy. Using a mixed stellar population model, we break our diffuse light into two populations: one at 10 Gyr, representing stars pulled from the host galaxies, and a younger component, whose age is determined by fitting the model to the data. We find similar ages for the young populations of both tails, (195^{+13}_{+0} and 170^{+70}_{+44} Myr for NGC 3256W and NGC 3256E, respectively), but a larger percentage of mass in the 10 Gyr population for NGC 3256E ($98^{+1}_{-3}\%$ vs $90^{+5}_{-6}\%$). Additionally, we detect 31 star cluster candidates in NGC 3256W and 19 in NGC 3256E, with median ages of 141 Myr and 91 Myr, respectively. NGC 3256E contains several young (< 10 Myr), low mass objects with strong nebular emission, indicating a small, recent burst of star formation.

Key words: galaxies: interactions – galaxies: individual: NGC 3256 – galaxies: star clusters: general

1 INTRODUCTION

Galaxy-galaxy interactions lead to the redistribution of stars and gas about each system, and an infusion of material into the local intergalactic medium, promoting star formation (Schweizer 1987). Tidal tails are signatures of galactic mergers (Schweizer 1978), illuminated by the ignition of star for-

mation (Schombert et al. 1990). Turbulent energy injected into the local H I through these mergers compresses the gas, forming new stars (Renaud et al. 2014); This is observationally shown in Mullan et al. (2013), who were able to link the presence of Star Clusters Candidates (SCCs) to turbulent regions of H I. While the young, in-situ formed SCCs of tidal tails have been studied in the past through imaging and spectroscopy (e.g. Knierman et al. 2003; Trancho et al. 2007; de Mello et al. 2011; Bastian et al. 2009; Mullan et

* E-mail: mrodru@psu.edu

al. 2011; Torres-Flores et al. 2012), the composition of the underlying stellar material remains a mystery.

We know that gas is easily extracted from the parent galaxies during interactions (e.g. Hibbard et al. 2001), but whether or not stars follow suit has not yet been established. The extracted gas can collapse to form stars in a clustered manner, yet at the same time, simulations have shown that clusters in tails can be easily disrupted (Kruijssen et al. 2011). This sparks an obvious question: what are tidal tails made of? What is the relative fraction of gas and old stars within the interaction ejecta? The answer can inform dynamical simulations of interactions, and therefore help refine our understanding of the enrichment of the intergalactic medium. In fact, current dynamical simulations (e.g. Renaud et al. 2009) use an older stellar component as a gravitational “anchor” for the gas. Is this requirement justified by the observations?

Existing studies have focused on the young stellar components of tidal tails, and therefore do not have the capability to probe deep into these regions. We have developed a new observing program designed to do just this, using deep, photometric *ugriz* imaging. To derive an accurate age estimate for a tidal tail, we plan our exposure times to view across the stellar sequence in our diffuse tidal tail light. These tails are imaged in each filter to an adequate signal to noise ratio, allowing us to derive an average colour and age of their diffuse light. This has the additional benefit of allowing us to age date star clusters within the tail.

We choose the twin tidal tails of NGC 3256 as a case study for our method. The system is relatively nearby at a distance of 38 Mpc (Knierman et al. 2003), with an interaction age of 400 Myr (Knierman et al. 2003) - not so young that our observations will be drowned out by OB stars, yet young enough so that the tidal structure is still visible. It has been well studied in the past through spectroscopic (Trancho et al. 2007; Trancho et al. 2007; Lípari et al. 2000), photometric (Mullan et al. 2011; Knierman et al. 2003; Zepf et al. 1999) and H α (English et al. 2003) observations, giving us benchmarks to compare to.

We will begin in Section 2 by describing our data and our reduction process. In Section 3 we describe our analysis methods, and in Section 4 we show our results. In Section 5 we discuss our findings, and conclude our paper with the main points of our research in Section 6.

2 DATA REDUCTION AND PROCESSING

2.1 Reduction

Images were obtained from the Gemini-South Observatory from March 2013 to June 2013, using the GMOS imager. The GMOS field of view is superimposed on an optical image from the Digital Sky Survey in Figure 1, measuring 5.6×5.6 arcmin. Exposure details are shown in Table 1.

Bias and flat field frames were provided by the observatory. Bias frames were taken every day, but flat fields were taken approximately once every 2 weeks. The flats closest to the observation date were used for flat fielding. We used IRAF for data reduction. Reduced images were mosaiced to obtain a single FITS file from the three CCDs. Combined frames from the *u*, *g*, and *r* filters were compiled together in

DS9 to create a composite colour image of each tail. Figure 2 shows colour frames of NGC 3256E and W. Science frames were calibrated using images of standard star fields (Smith et al. 2002) taken each night.

2.2 Fringing

Fringing is caused by thin-film interference effects in the CCD array as photons are reflected within the array. This effect is largely seen in the longer wavelengths, where the optical depth of photons through the silicon detector is large enough to allow photons to reflect off the back of the structure and interfere with incoming photons. Since the interference is dependent on the thickness of the detector, the fringe pattern will remain nearly constant, although it can vary over time in intensity.

Both the *i*-band and the *z*-band were severely affected by fringing. Fringe frames provided by the observatory, containing the fringing pattern, allowed for its removal. Unfortunately, the fringing in the *z*-band was too severe and could not be corrected. Data in the *z*-band are therefore not used in our analysis. For the *i*-band, a median combined frame, compiled from several fringe frames, was needed to adequately subtract the pattern. Results of the fringe removal for the Western tail are shown in Figure 3.

Although the fringing pattern was removed, *i*-band data in the Western tail was left with a slight gradient across the image. This is an effect of the subtraction process and imperfect fringe frames, and can affect our measurements of diffuse light in the *i*-band. Data for the Eastern tail does not show this gradient.

2.3 Masking Images

Effective Low Surface Brightness (LSB) photometry requires the elimination of contaminant sources. We are attempting to observe the dim, diffuse light of the tidal tail, but light from foreground stars and background galaxies can easily dominate. It is necessary to mask these sources from our images before performing analysis. Masking the images involves three steps: masking point sources, masking diffuse sources, and masking bad pixels.

2.3.1 Magnitude Masking

To determine how far the influence of a point source object will extend, we create fake stars using *addstar* given a psf generated with the task *psf*. Bright, isolated stars are used to create the template psf. Stars are added to the tail and photometry is performed using the sum of all points inside a list of apertures. The same process is performed on the original image of the tail with no additional stars, and the two sum values are compared to each other for each aperture radius. The radius at which the precision *P* is less than 0.001 is given as the masking radius, where the precision is defined as:

$$P = \frac{|\Sigma_{\text{stars}} - \Sigma_{\text{tail}}|}{\Sigma_{\text{tail}}} \quad (1)$$

This radius is plotted against the magnitude of the added stars and a linear magnitude-radius relationship is found using the IDL procedure *linfit.pro*. This process

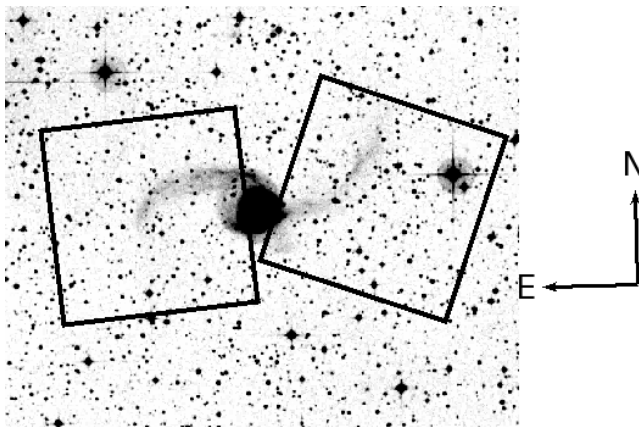


Figure 1. Scanned blue image of NGC 3256 from the Digital Sky Survey. The GMOS field of view is shown in black boxes, and measures 5.6×5.6 arcmin.

Tail	Filter	Number of exposures	Exposure time per frame (single pointing) (s)	Observation date(s)
West	<i>u</i>	13	600	March 17, 2013; April 13, 2013
West	<i>g</i>	6	150	May 11, 2013; June 3, 2013
West	<i>r</i>	3	150	May 11, 2013
West	<i>i</i>	5	200	May 11, 2013
East	<i>u</i>	13	600	March 12, 2013; March 13, 2013
East	<i>g</i>	3	150	March 17, 2013
East	<i>r</i>	3	150	March 17, 2013
East	<i>i</i>	5	200	March 17, 2013

Table 1. Exposure numbers and times for the Eastern and Western tail. Also listed are dates covering our observations. Data for the *z*-band is excluded (see Section 2.2).

has the weakness that light from the added stars cuts off at a radius defined by the parameter *psfrad* in *daopars*. This makes it impossible to add bright stars ($m \approx 20$) for our analysis, as the light does not drop below a precision of 0.001 earlier than *psfrad*. Faint stars must be used instead, and we extrapolate the masking radius to brighter magnitudes, using the linear magnitude-radius relationship.

Objects are found in the image frames using the IRAF task *daofind*. One frame in each filter is used to find the object coordinates, which are then used for every other image in the filter. Photometry is performed using *phot* in IRAF with an aperture radius of 6 pixels. We apply a mask to objects with magnitudes less than 25, to protect against spurious detections. This will include objects identified as SCCs.

Note that this procedure will not work for saturated objects, as their magnitudes cannot be accurately calculated. The masking will be underestimated, and a manual radius will need to be set. Fortunately, this was only needed for 7 objects in the Western tail, and none in the Eastern.

2.3.2 Object Masking

The IRAF task *objmask* will find objects in an image which are $n \cdot \sigma$ above background. This is useful for detecting cosmic rays and non point source objects (e.g., resolved galax-

ies). It is set to detect objects which are a minimum of 2 pixels in size to account for cosmic rays.

2.3.3 Bad Pixel Masks

The Gemini IRAF package includes a set of pixel masks for detectors at both the North and South sites. However, streaks in the images appear in several consistent locations which are not covered by the pixel masks. A new mask is created with manual corrections for these streaks. This mask has the same shifts applied to it as the aligned images, resulting in a unique bad pixel mask for every image.

The three masks are compiled into one composite image which is multiplied by every science frame. An example of this process is shown in Figure 4.

3 DATA ANALYSIS

3.1 Low Surface Brightness Photometry

Use of the image masks will eliminate contaminant sources, leaving the diffuse light of the tail untouched. The background level of the sky must be accurately measured and subtracted from the tail to find its surface brightness.

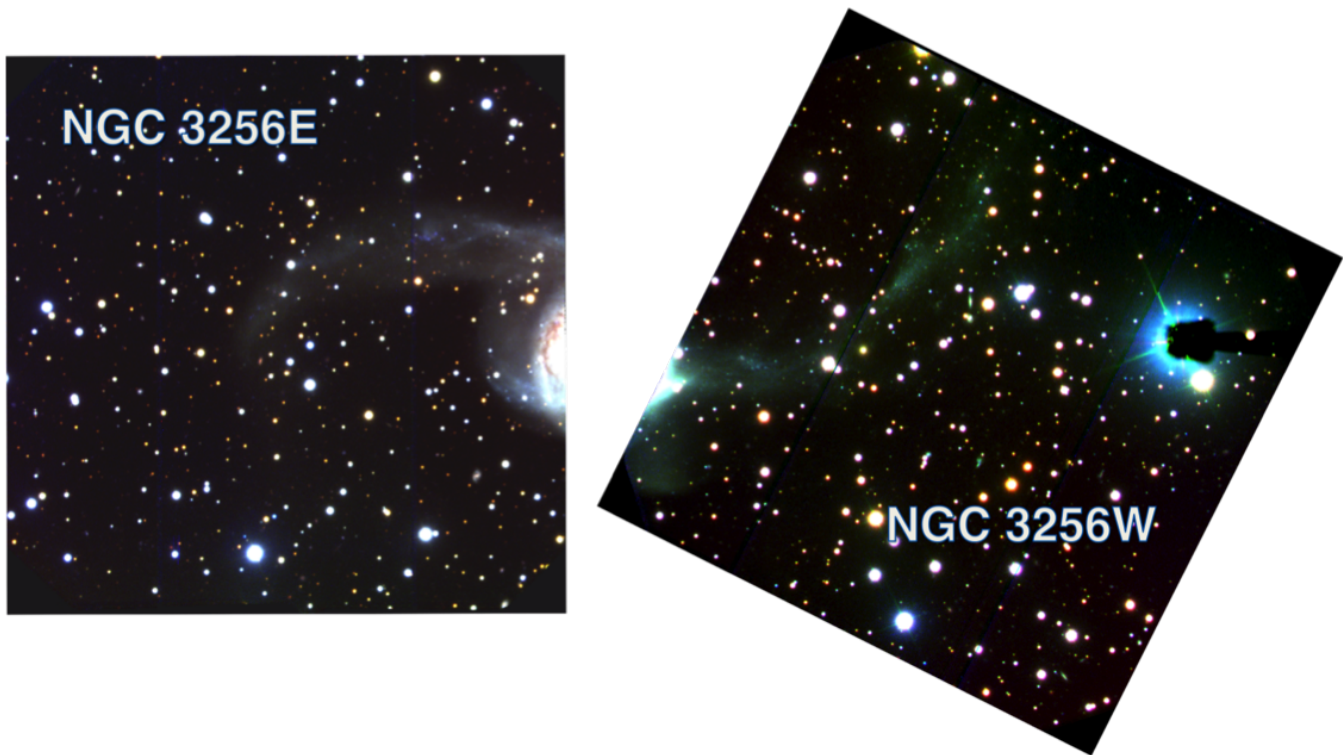


Figure 2. Colour images of NGC 3256E (*left*) and NGC 3256W (*right*) taken with GMOS-S. Combined images in the *u*-band represent blue, *g*-band images represent green, and *r*-band images represent red. In this image, North is up, and East is to the left.

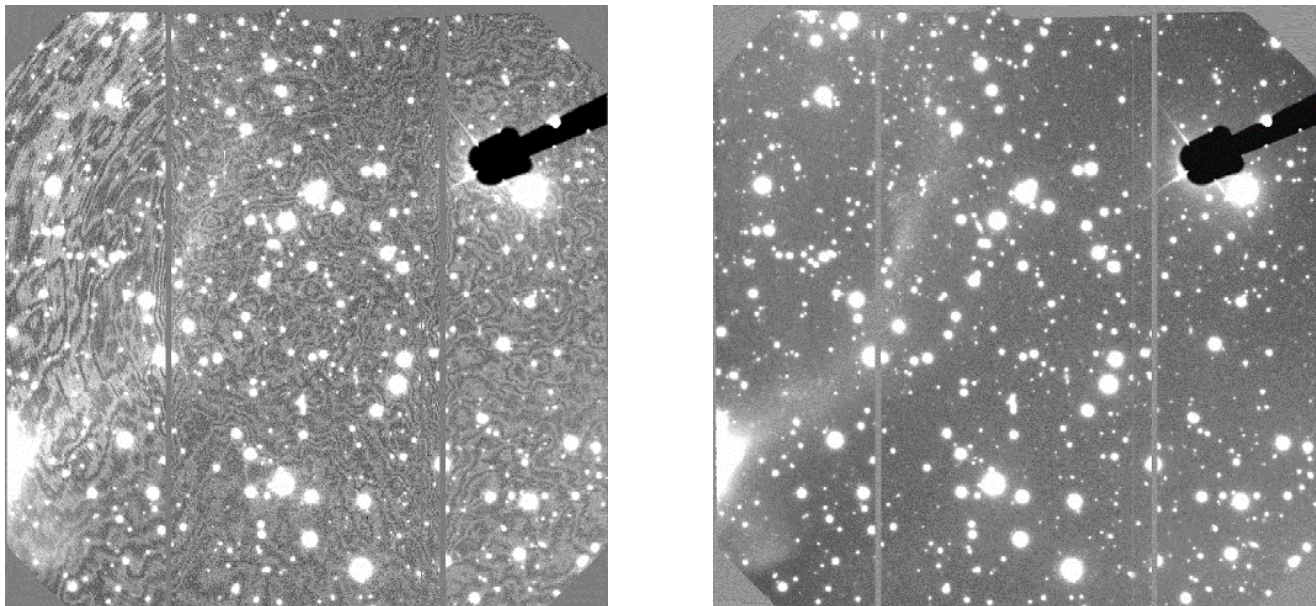


Figure 3. *Left:* *i*-band image of the Western tail prior to fringe removal. The shadow of the telescope’s wavefront sensor can be seen in the upper right. *Right:* Same image after the fringe pattern has been removed. Note the residual gradient across the image, resulting in bright patches at the upper left and lower right corners.

3.1.1 Background determination

The GMOS detector consists of three E2V CCDs. Each of these chips has a background level differing from the others. We sample 25 unique locations on each chip with square apertures of dimensions 41×41 pixels, or 6×6 arcsec-

onds. Locations are selected to be near the tail to achieve representative sampling.

We fit the data to a Gaussian distribution using a maximum loglikelihood estimator. Initial guesses at the mean and standard deviation values are found by plotting the data in a histogram and fitting the binned points to a Gaussian curve

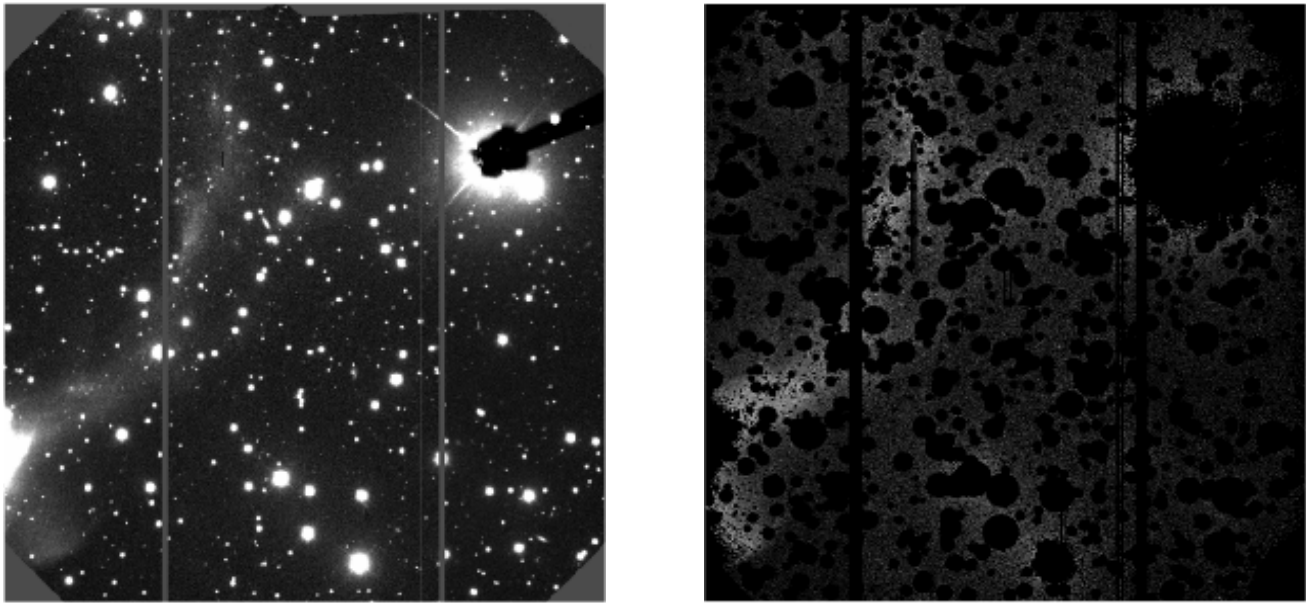


Figure 4. *Left:* g -band image of NGC 3256W. *Right:* Same image, but with the mask applied. The tail light stands out free of contaminant sources. Note the diffuse light from several brighter stars appears in the top and bottom of the image. These objects were saturated and an accurate mask could not be found. However, they are far enough from the tail to not have an effect.

using the IDL program `gaussfit`. As this method is sensitive to the size of the histogram bins, we use this as first approximation and perform our final analysis with the more robust maximum loglikelihood estimator.

3.1.2 Tail Definition

Images in the g -band were combined for defining tail regions using `imcombine`, prior to masking. We chose g -band data as it offered the best seeing and a good signal to noise. The combined frames were then smoothed with a Gaussian kernel with a FWHM of 5-6 pixels, in order to boost the S/N in each pixel. Regions defined as “in-tail” were determined as contiguous regions 3σ above the background, using the IDL program `find_boundary.pro`. Average background and standard deviation values were determined in each chip from the co-added image. Regions between adjacent chips were manually added to extend the tail across the CCDs.

For the Eastern tail, we manually cut the region to exclude the bulge and southern tidal debris, so as to focus on the tail itself. Another cut was made at the tip of the tail to exclude regions marked by diffuse light from a nearby bright star. The Western tail also includes a manual cut on the south-eastern edge to exclude an extended region due to diffuse light from bright stars. Figure 5 contains our boundaries considered for photometry. Observations for the Western tail include a diffuse feature seen at the bottom of the image, separate from the tail (see Figure 5). We include measurements for this region, but consider it separately from the tail itself.

3.1.3 Photometry

We apply a grid of boxes 50×50 pixels in size to both tails for our measurement apertures of diffuse light, as show in Figure 5, allowing us to determine the spatial distribution of colours in the tail. Box sizes correspond to 7.3×7.3 arcseconds on the sky, or 365×365 pc on the tail. The tail boundaries are shown in blue. Several boxes are not fully bounded inside the blue tail boundary, however, only the pixels within the tail in these boxes are counted for photometry. We limit analysis to boxes with ≥ 50 pixels within the tail. For NGC 3256W we mark the boundary between the diffuse structure and tail itself in cyan.

We apply a 3σ limit to our detections. The flux in each measurement box was corrected for airmass and Galactic dust extinction. Foreground extinction corrections were obtained from Schlafly & Finkbeiner (2011), using an $R_\lambda = A_\lambda/E(B-V)$ reddening law, with $R_V = 3.1$. The corrected flux was averaged across images in the filter and converted to a surface brightness in units of $\text{mag} \cdot \text{arcsec}^{-2}$. Magnitude zero points and airmass correction coefficients were taken from the Gemini Observatory webpage¹, and are listed in Table 2.

3.2 Cluster Photometry

NGC 3256 is far enough away, at 38 Mpc, that its clusters will not be resolved from the ground, and will appear as point sources. For a typical seeing of $0.9''$, objects less than 74 pc will appear unresolved. Thus, our photometry will be performed on these unresolved, point sources.

¹ <https://www.gemini.edu/?q=node/10445>

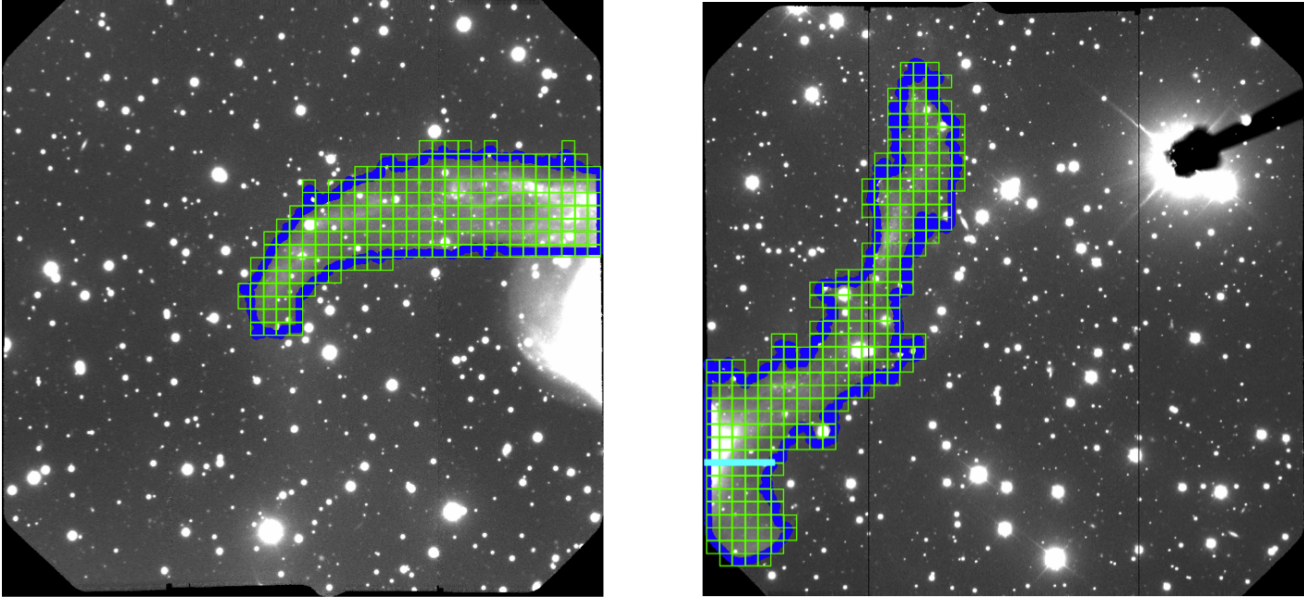


Figure 5. Selected regions for photometry for NGC 3256E (*left*) and NGC 3256W (*right*). Blue lines indicate the boundary of the tail region. In the Western tail, a cyan line indicates the boundary between the tail and diffuse structure. Several boxes are not fully enclosed with the tail, however only pixels within the blue boundary are counted for photometry. We additionally only count boxes with ≥ 50 good pixels.

Filter	Magnitude zero point	Airmass correction coefficient
<i>u</i>	24.91	0.38
<i>g</i>	28.33	0.18
<i>r</i>	28.33	0.10
<i>i</i>	27.93	0.08

Table 2. Magnitude zero points and airmass correction coefficients for the E2V CCDs

3.2.1 Aperture Corrections

The imaging field is crowded enough to require aperture corrections to prevent contamination from outside objects. A curve of growth analysis using 10 bright stars was performed for each filter. Given the varying PSF of each image, it was necessary to extend this analysis to every image, so that each image has its own aperture correction. We corrected for a measurement radius of 6 pixels, for every image. For reference, the FWHM of our images ranged from ~ 4.5 pixels, to ~ 9.5 pixels, depending on the seeing.

3.2.2 Photometry

Objects were detected in *g*-band combined images using the IRAF task *daofind*. Sources were labeled as “in-tail” or “out-of-tail” using boundaries as defined in section 3.1.2. Detections that were cosmic rays, saturated stars, resolved galaxies, or duplicate detections were manually removed. Figure 6 shows locations of detected objects.

We used the IRAF task *phot* to perform aperture photometry on our detected objects, with an aperture size of 6 pixels. We considered sources $> 3\sigma$ above the background. To remove cosmic rays in our frames, we used the IDL routine *la_cosmic* on our dataset. Objects containing cosmic

rays in their measurement aperture were discarded for that particular frame.

4 RESULTS

4.1 Tidal Tail Colours

Integrated surface brightness, colour, and age measurements are included in Table 3. We plot colours for the West and East tails in Figure 7. An extinction vector of $A_V = 0.5$ is shown. Data for regions within the diffuse structure in the Western tail are shown in orange, while measurements from regions in the tail itself are shown in green. In the right panel, the colours of the different regions of the Eastern tail are shown in purple. The overall tail colours from Table 3 are marked by yellow “X’s”. We plot these colours against Simple Stellar Population (SSP) evolutionary models from Marigo et al. (2008) for a metallicity of $1.5 Z_\odot$ and a Salpeter (Salpeter 1955) IMF, in solid black. Our choice in evolutionary models follows Konstantopoulos et al. (2012), which found good fits between Marigo et al. (2008) models and their data, for young and old clusters. Our motivation for this metallicity comes from Trancho et al. (2007), who spectroscopically studied a number of in situ formed star clusters in NGC 3256 and found a mean metallicity of $1.5 Z_\odot$. Overlaid on data for the Western tail are tracks for a Kroupa and Chabrier IMF at $1.5 Z_\odot$. For the Eastern tail, we show evolutionary tracks of 1, 1.5, and $2 Z_\odot$ using a Salpeter IMF. The similarity of evolutionary tracks using different IMFs and metallicities suggest these will have little effect on our analysis.

Results for the Eastern tail are in good agreement with measurements from Mulia et al. (2015), which studied the Eastern tail of NGC 3256, among other tails. A comparison of ages in Table 3 shows the integrated diffuse light in the

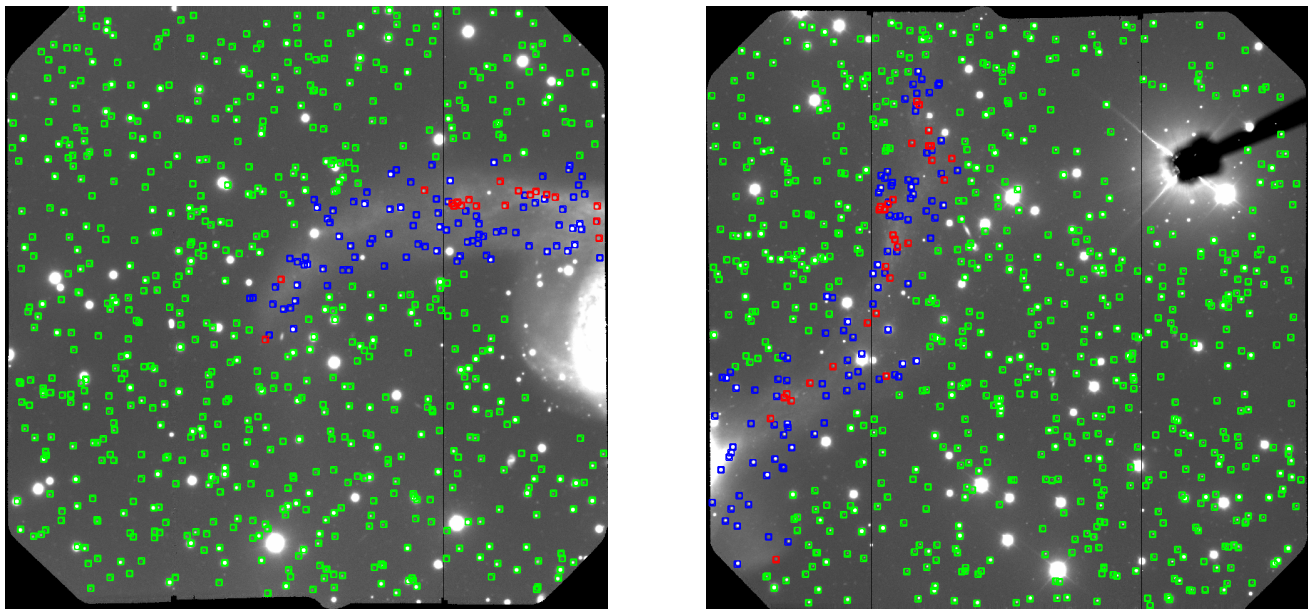


Figure 6. *Left:* Locations for in-tail objects (blue) and out-of-tail objects (green) shown for NGC 3256 E. Red sources are Star Cluster Candidates (SCCs), as determined in Section 4.3.1. *Right:* Same, but for the Western tail.

Tail	u (mag arcsec $^{-2}$)	g (mag arcsec $^{-2}$)	r (mag arcsec $^{-2}$)	i (mag arcsec $^{-2}$)	$u-g$	$r-i$	Diffuse Light Age (Myr)	Interaction Age ¹ (Myr)
West	25.59 ± 0.05	24.54 ± 0.05	24.22 ± 0.05	24.09 ± 0.05	1.05 ± 0.07	0.13 ± 0.07	288^{+11}_{-54}	400
East	25.49 ± 0.05	24.23 ± 0.05	23.77 ± 0.05	23.51 ± 0.05	1.26 ± 0.07	0.26 ± 0.07	841^{+125}_{-157}	400

Table 3. Measured properties of NGC 3256. Note that these values are *not* averages, but are instead found by integrating the tail light with the boundaries shown in Figure 5 as a whole. Photometry errors are negligible, due to sampling the large area of the tidal tail. We estimate systematic errors at a minimum of ± 0.05 mag.

¹From Knierman et al. (2003)

Eastern tail is more than twice as old as the interaction age of the galaxies, suggesting the stellar light in the Eastern tail is dominated by an older stellar population, likely originating from the host galaxies. To investigate this, we add light to our SSP model from a stellar population at 10 Gyr and solar metallicity, creating a Mixed Stellar Population (MSP) model. The influence of the old population reddens both the $u-g$ and $r-i$ colours. We choose SSP models with 4 logarithmic ages (8.0, 8.2, 8.4, and 8.6 log yrs) to demonstrate this effect, by plotting their progression towards redder colours as we increase the mass ratio between the 10 Gyr population and this original SSP (see top left of Figure 8).

In the top right of Figure 8 we fit an MSP model to the tail’s integrated colour. The ratio of masses between the populations is adjusted to minimize the distance between the MSP track and the integrated tail colour. We can then find the age of the original SSP model corresponding to these colours to obtain a representative age of the young population. We find the best fit parameters give a young population at an age of $8.23^{+0.23}_{-0.11}$ log yrs and a mass ratio $M_{\text{old}}/M_{\text{young}}$ of $46.6^{+87.1}_{-25.8}$, indicating that $98^{+1}_{-3}\%$ of the stellar mass and $68^{+11}_{-13}\%$ of the bolometric flux is from a 10 Gyr population. Upper and lower limits are found by fitting our MSP track to the upper and lower limits of the integrated $u-g$ and $r-i$ colours. This can result in smaller upper limits and larger

lower limits for our mass and flux ratios, as the older ages require less of a 10 Gyr population to shift the track in the appropriate manner. If instead of a 10 Gyr population we included an 8 Gyr population, the mass ratio $M_{\text{old}}/M_{\text{young}}$ would increase to 48.7, while a 12 Gyr population would increase $M_{\text{old}}/M_{\text{young}}$ to 47.5. Note that while the mean colours of the tail are fit to a specific population, several regions in the tail can be fit to younger ages at varying mass ratios. In the bottom panels of Figure 8 we include MSP models with young population ages of 8.2 and 8.6 log yrs. Our fit to 8.6 log yrs represents the oldest possible age for new star formation, as stars at this age would have formed immediately after the interaction. This also gave us the minimum mass ratio between the populations as $M_{\text{old}}/M_{\text{young}} = 6.4^{+3.8}_{-2.9}$. Although the exact numbers vary with location in the tail, and depend on assumptions about the ages of the young and old populations, we have demonstrated that there is a significant contribution from an old stellar population to the diffuse light in the Eastern tail.

Our fits to the MSP models assume $A_V = 0$. We do not expect the role of extinction to be large, as discussed at the end of Section 5. We note that the effect of dust would be to decrease the age and mass ratio $M_{\text{old}}/M_{\text{young}}$ of the tail, as the data would shift closer to the SSP track, toward bluer colours.

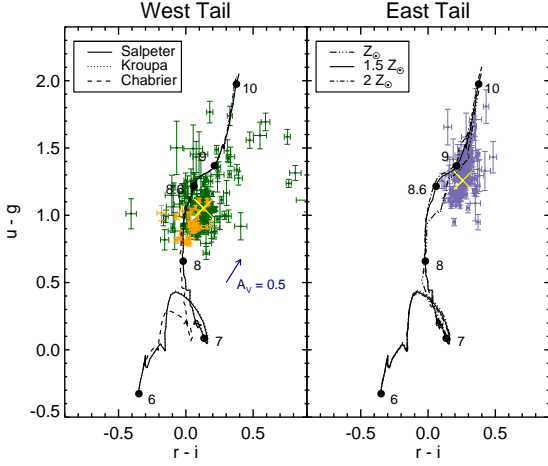


Figure 7. Colour-colour plot of NGC 3256W (*left*) and E (*right*). Points correspond to integrated light from green boxes in Figure 5. Green and purple points mark data from the Western and Eastern tails respectively, while orange points for NGC 3256 indicate data from the separate diffuse structure. Numbers mark the logarithmic age of the model from 1 Myr to 10 Gyr. A yellow “X” marks each tail’s overall colour. In each plot we include a $1.5 Z_{\odot}$ SSP evolutionary track with a Salpeter IMF as a solid black line. On the left, we include tracks using Kroupa and Chabrier IMFs, at $1.5 Z_{\odot}$, to highlight the insensitivity of the modeled colours to the choice of IMF. On the right, we include tracks with a range of metallicities to again highlight the minimal effect of metallicity on colour.

We perform the same analysis on the Western tail in Figure 9. The best fit mass ratio is $M_{\text{old}}/M_{\text{young}} = 9.4^{+8.1}_{-4.2}$, with an age of $8.29^{+0.03}_{-0.0}$ log yrs. However, photometric errors in the i -band can inflate the mass ratio between the old and young populations. The effect of the old population on the $r-i$ colour is to push data points toward redder colours. Unfortunately, this same effect could also be caused by photometric scatter from imperfect fringe frame removal. As noted in Section 2.2, fringes in the i -band were removed, but a gradient was left across the images. This gradient could have artificially reddened our $r-i$ colours, which would increase the mass ratio $M_{\text{old}}/M_{\text{young}}$, creating a larger old population than truly exists. We note this has a marginal effect on the *age* of the light (at $8.29^{+0.03}_{-0.0}$ log yrs), as the $u-g$ colour is primarily used to determine the age, which is clearly dominated by the younger population in this tail.

4.2 Tail Stellar Mass

The stellar mass of each tail region can be calculated using its observed $M_{\text{old}}/M_{\text{young}}$ ratio and the magnitude in each filter. We are over-constrained, as we will have a unique mass for each filter’s magnitude. We take the mean value between filters to use as our mass, and repeat this process for each measurement box shown in Figure 5. Each data point is broken into a composite population, one part consisting of a 10 Gyr population, and the second a younger population, whose age and mass ratio relative to the old population is determined by the MSP fit to the data point. Upper and lower bounds on our masses are found by fitting our MSP model to

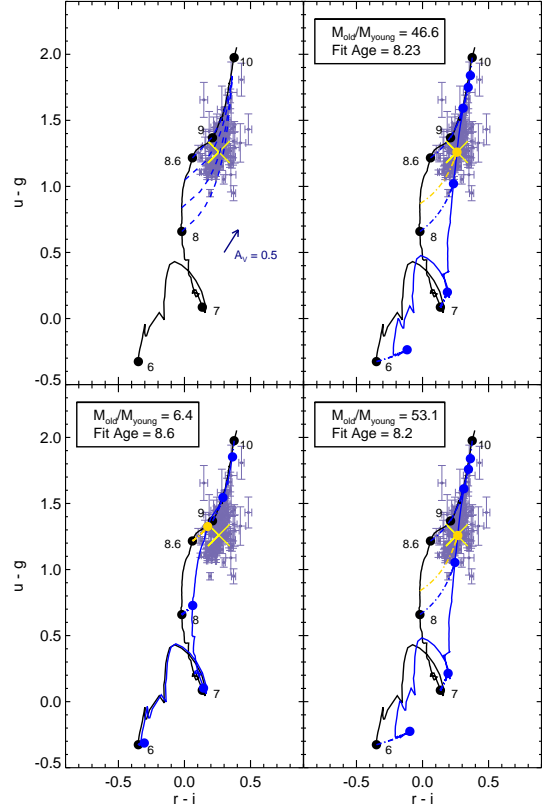


Figure 8. *Upper Left:* Dashed blue lines indicate the shift in evolutionary track colours for specific young population ages (8.0, 8.2, 8.4, 8.6 log yrs), as the ratio of $M_{\text{old}}/M_{\text{young}}$ increases, where the old population is a 10 Gyr stellar population. *Upper Right:* Best fit MSP evolutionary track (blue) to overall tail colours, at a mass ratio of $M_{\text{old}}/M_{\text{young}} = 46.6$. Gold circle marks the closest point between the track and the tail colour, corresponding to an age of 8.23 log yrs. *Bottom:* MSP fits to tail colour at specified logarithmic ages. The mass ratios are adjusted to find the minimum distance between the tail colour and the MSP track colour at the indicated young population age (8.6 and 8.2 log yrs). Gold circle indicates the point on the MSP track corresponding to the age which is being fit.

the upper and lower error bounds of each data point. This can create smaller upper bounds and larger lower bounds than the nominal values, as the best fit model may require different mass ratios between the two populations. We compare the masses of each tail to previous measurements of HI, and our observed total cluster mass as derived in the ensuing section, in Table 4. We use a Salpeter IMF to derive our mass values. While the choice of IMF does not affect the colours of our objects (and therefore our age derivation), it can have an appreciable effect on the derived masses. A Chabrier (Chabrier 2001) or Kroupa (Kroupa 2001) IMF results in a decrease in mass by a factor of ~ 2 relative to a Salpeter IMF.

Our masking of contaminant sources has eliminated a substantial fraction of each tail. In the Western tail, unmasked pixels represent 41% of the total tail area; for the Eastern tail, we have 54% of the tail left unmasked. We correct our masses of diffuse light in Table 4 to account for the missing tidal tail light.

Several data points younger than the interaction age of

Tail	Diffuse Old Age (log yrs)	Diffuse Young Age (log yrs)	Median Cluster Age (log yrs)	Diffuse Old Mass ($10^8 M_\odot$)	Diffuse Young Mass ($10^8 M_\odot$)	Star Cluster Mass ($10^8 M_\odot$)	H I Mass ¹ ($10^8 M_\odot$)
West	10	$8.29_{+0.0}^{-0.03}$	8.15	$128.3_{-5.6}^{+5.6}$	$15.1_{-0.5}^{+0.5}$	$0.31_{-0.06}^{+0.05}$	22.0
East	10	$8.23_{+0.11}^{-0.23}$	7.96	$392.2_{+6.1}^{-2.8}$	$10.7_{-1.3}^{+1.3}$	$0.13_{-0.02}^{+0.04}$	14.0

Table 4. Mass measurements of NGC 3256, using a Salpeter IMF for stellar mass.

¹From Knierman et al. (2003)

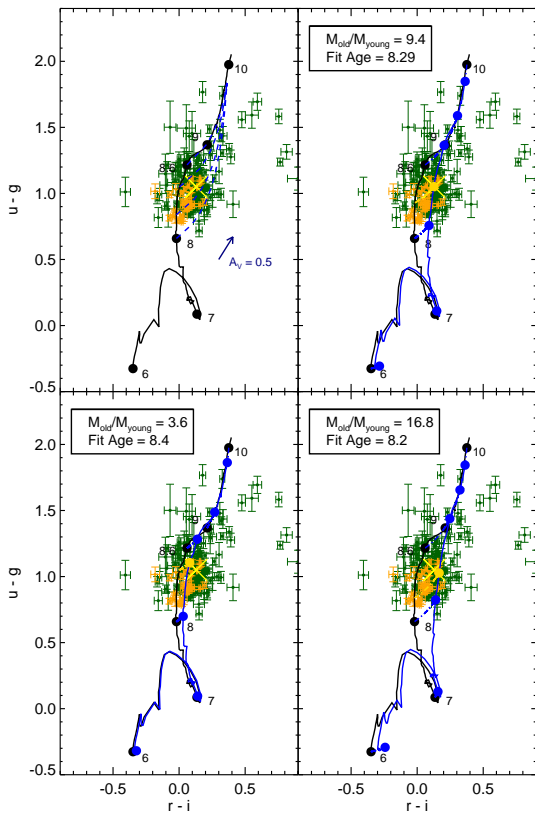


Figure 9. Same as Figure 8 but for the Western tail.

8.6 log yrs in the Western tail fall directly on the SSP track. In these cases our colour-colour diagram indicates the mass is completely derived from a young population, with negligible contribution from an old population. More likely, the presence of the old population is drowned out by the flux of the young population. To find the maximum old population allowed in such cases, we add the maximum allowed mass such that the derived magnitude fits within each filter observed magnitude error bars. This marginally increases the overall mass of the tail by an additional 0.2%.

4.3 Star Clusters

4.3.1 Cluster Colours

Colour-colour diagrams for point sources detected in the Western and Eastern tails are shown in Figures 10 and 11, respectively. We compare the distribution of sources both in and out of the tail.

Locations for detected sources are shown in Figure 6. Following the above standard, we superimpose a Salpeter

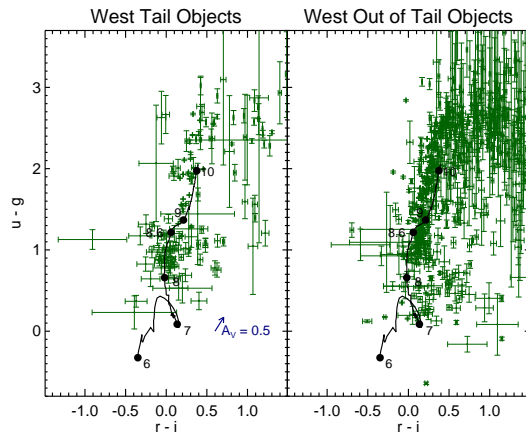


Figure 10. Objects detected by *daofind* both in the Western tail (*left*) and outside the tail (*right*). We zoom out in this plot and decrease the plot symbol size to highlight the wide colour range of objects detected.

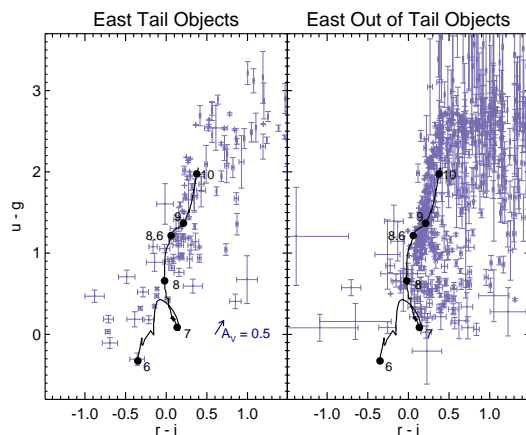


Figure 11. Same as Figure 10 but for the Eastern tail.

IMF at $1.5 Z_\odot$. An over density of objects can be seen in both tails (see Figures 10 and 11) as compared to their out-of-tail sources, at and below the 8.6 log yrs marker, suggesting that many of these objects are real clusters. We can see the Western tail has more of these objects, although the Eastern tail has a grouping of several very young objects. However, in-tail and out-of-tail sources for both tails greatly overlap. To aid in discriminating between contaminating and SCC sources in our tails, we use $g-i$ and M_g cuts as in Knierman et al. (2003) and Mullan et al. (2011). We plot

colour-magnitude diagrams in Figure 12 overlaid with SSP models using a Salpeter IMF for masses of 10^4 and $10^6 M_{\odot}$. Colours of data points indicate their $u-g$ values.

Both of the out-of-tail plots show an excess of sources greater than $g-i = 0.5$. A second clustering on the faint end is seen at $g-i < 0.5$ and $M_g < -9.25$. A final cut at $M_g < -11.5$ is made to exclude brighter contaminating sources. We thus consider objects with $g-i \leq 0.5$ and $-11.5 \leq M_g \leq -9.25$ to be star cluster candidates (SCCs).

We present the number of SCCs detected within ($N_{\text{in}}^{\text{SCC}}$) and outside ($N_{\text{out}}^{\text{SCC}}$) the tail, as well as the areas of each region (A_{in} and A_{out}) in Table 5. In-tail SCC excess Σ_{SCC} is defined as the difference between $N_{\text{in}}^{\text{SCC}}/A_{\text{in}}$ and $N_{\text{out}}^{\text{SCC}}/A_{\text{out}}$. Poisson errors are given at 1σ , recorded from $N_{\text{in}}^{\text{SCC}}$ and $N_{\text{out}}^{\text{SCC}}$. SCC excess in the Western tail is significant at $> 5\sigma$, while the Eastern tail excess is significant at 4σ , suggesting most of these objects are real clusters. Our results for the Western tail agree with Mullan et al. (2011), which found a statistically significant excess, although at a lower confidence level. However, they found no significant excess in the Eastern tail. Our values differ mainly for two reasons: our colour and magnitude cuts are more conservative, and our sample area for the out-of-tail region is larger. Mullan et al. (2011) used a colour-magnitude criteria of $V-I < 2.0$ ($g-i \approx 2.2$, determined through fitting Marigo et al. 2008 SSP models) and $M_V < -8.5$ ($M_g \approx -8.2$). However, when looking at Figure 12, we see a large number of out-of-tail objects which pass these thresholds, indicating we require tighter restraints on our cuts. This leads to fewer objects which meet our SCC criterion, but improves the statistics on our background level estimate, $N_{\text{out}}^{\text{SCC}}/A_{\text{out}}$.

A colour-colour diagram with only these SCCs is shown in Figures 13 and 14. Overlaid in gray are data points for the diffuse light of the respective tidal tail. The SSP models from Marigo et al. (2008) do not include nebular emission. However, the nebular continuum, as well as emission lines from $H\alpha$, $H\beta$, $[\text{O III}]$ and $[\text{O II}]$, can have strong effects on our colours for young objects, with ages < 10 Myr. We use *Starburst99* (Leitherer et al. 1999) to include a nebular continuum, as well as emission from $H\alpha$ and $H\beta$. Following Gallagher et al. (2010) and Fedotov et al. (2011), we find the strengths of the $[\text{O III}]$ and $[\text{O II}]$ lines from the KISS sample of nearby low-mass star-forming galaxies (e.g., Salzer et al. 2005). We use the median ratios of $[\text{O III}]/H\beta$ and $[\text{O II}]/H\beta$, listed at 0.08 and 0.56, respectively. $H\alpha$ emission falls in the r filter, causing the $r-i$ colour to appear bluer. Both $H\beta$ and $[\text{O III}]$ fall in the g -band, while $[\text{O II}]$ is in the u -band. Depending on the relative strengths of the oxygen lines, this can cause the $u-g$ colour to become bluer or redder. To show a possible range of nebular emission, we also include a track setting $[\text{O III}]/H\beta$ to its 90th percentile value (0.66) and $[\text{O II}]/H\beta$ to its 10th percentile value (0.22). This provides a better fit for several data points in the Eastern tail, although the position of these clusters on the diagram is likely due to a combination of varying emission line strengths and dust extinction.

In examining Figure 13, we see a clear overdensity of SCCs in the Western tail compared to objects outside of the tail. In the Eastern tail (14), a number of SCCs exist at blue values of $u-g$ and $r-i$ which are distinct from those outside the tail. SCCs in the Western tail overlap with the diffuse light (though skewed to the blue end), while those in the

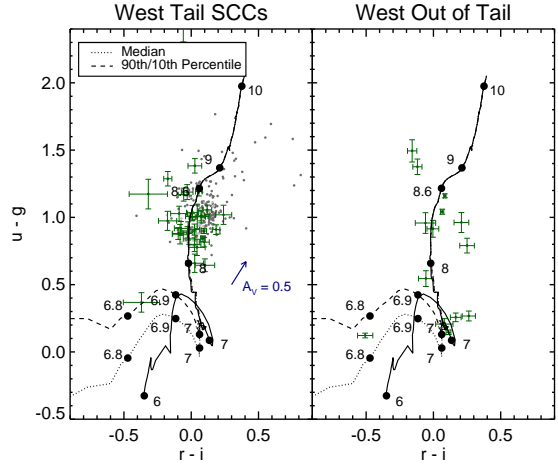


Figure 13. Star cluster candidates (SCCs) for the Western tail, as defined by colour cuts of $g-i \leq 0.5$ and $11.5 \leq M_g \leq 9.25$. Gray points correspond to diffuse light. For comparison, we show colours of objects outside the tail region on the right. Nebular tracks with emission from $H\beta$, $H\alpha$, $[\text{O III}]$, $[\text{O II}]$, and continuum emission are included. Dotted lines indicate median values of $[\text{O III}]/H\beta$ and $[\text{O II}]/H\beta$ emission, while dashed lines indicate the 90th and 10th percentile of $[\text{O III}]/H\beta$ and $[\text{O II}]/H\beta$ emission, respectively, from the KISS galaxy sample. 31 SCCs are detected in the Western tail, with a median age of 8.15 log yrs.

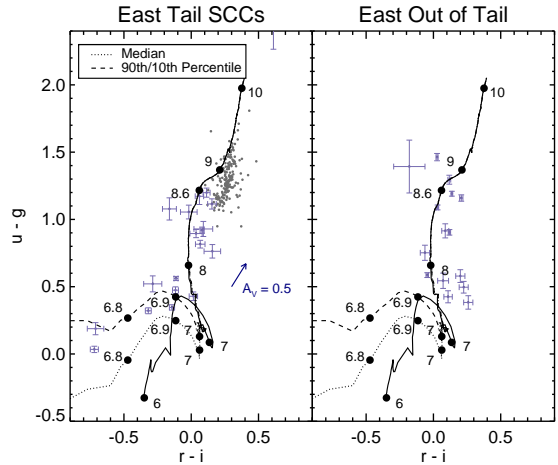


Figure 14. Same as Figure 13 but for the Eastern tail. Several young objects show strong nebular emission. 19 SCCs are detected in the Eastern tail, with a median age of 7.96 log yrs.

Eastern tail are distinct from the diffuse light in the host tail. To quantitatively test this, we apply the Kolmogorov–Smirnov (KS) test to the colour distribution of the diffuse light and SCCs. This test allows us to determine the probability that two samples were drawn from independent distributions. A p -value of less than 0.013 indicates the populations are distinct from one another at more than a 2.5σ confidence level. For the $u-g$ colours, we find p -values of 0.028 and 4.2×10^{-11} for the Western and Eastern tails, respectively. For the $r-i$ colours, we have p values of 3.9×10^{-5}

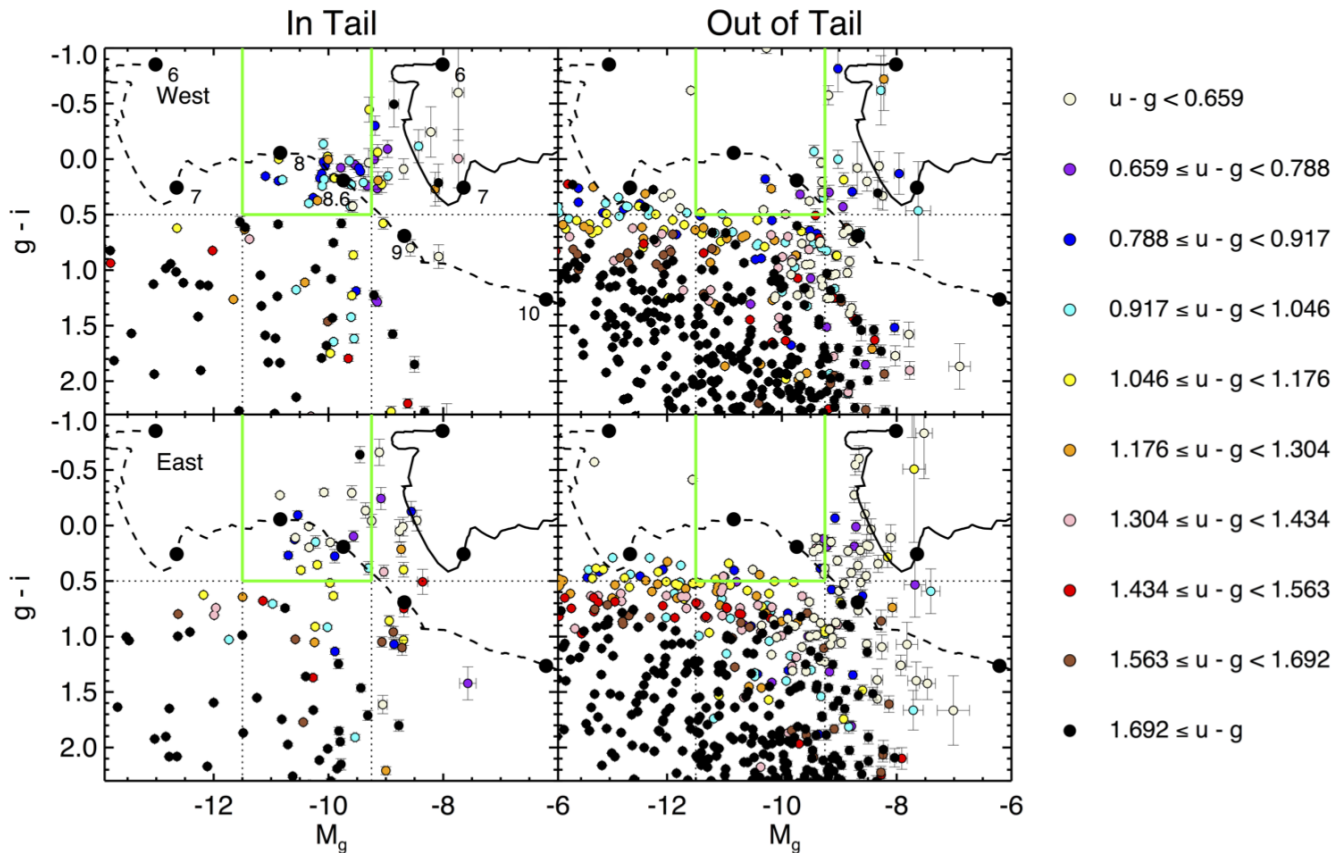


Figure 12. Colour-magnitude diagrams for the tidal tails. *Upper:* Data for the Western tail. Left hand panel shows sources in the tail, while objects outside of the tail are shown on the right. Colours of sources indicate their $u - g$ values. Overlaid are evolutionary tracks for 10^4 (solid) and 10^6 (dashed) M_{\odot} . Dotted lines indicated magnitude and colour cuts. Objects considered to be SCCs lie within the green box. *Lower:* Same, but for the Eastern tail.

Tail	$N_{\text{in}}^{\text{SCC}}$	$N_{\text{out}}^{\text{SCC}}$	A_{in} (kpc ²)	A_{out} (kpc ²)	$N_{\text{in}}^{\text{SCC}}/A_{\text{in}}$ (kpc ⁻²)	$N_{\text{out}}^{\text{SCC}}/A_{\text{out}}$ (kpc ⁻²)	Σ_{SCC} (kpc ⁻²)
West	31	14	301.38	2855.21	0.103	0.0049	0.098 ± 0.019
East	19	15	305.54	3019.22	0.061	0.0050	0.056 ± 0.014

Table 5. SCC counts for those detected within and outside the tail region. SCC excess (Σ_{SCC}) is defined as the difference between $N_{\text{in}}^{\text{SCC}}/A_{\text{in}}$ and $N_{\text{out}}^{\text{SCC}}/A_{\text{out}}$. Error bars of 1σ from Poisson statistics are shown. SCC excess in the Western tail exceeds 5σ , while the Eastern tail exceeds 4σ , showing statistically significant values of Σ_{SCC} in both tails.

and 8.4×10^{-13} , for the Western and Eastern tails. These results show the diffuse light and SCC colour distributions are distinct from each other in both tails.

4.3.2 Cluster Masses and Ages

Ages and masses of our sources are found using the 3DEF method (Bik et al. 2003). This uses a maximum likelihood estimator to find the ages and masses of each cluster, by adjusting the colour excess $E(B - V)$ to fit the observed colour in each filter to a given SSP evolutionary model. Results for the total masses and median ages of SCCs are shown in Table 4, with masses and ages shown in Figure 15; dashed lines represent our SCC detection limits based on our colour and magnitude criteria from Section 4.3.1. Error bars show the maximum and minimum age and mass for each data

point. At low masses, there are several points which do not fall within the detection band. These objects are subject to internal extinction, which dims them to fall within our SCC colour and magnitude cutoffs. There is a gap in age between the young objects in the Eastern tail and the main distribution with ages of 8.0 - 8.8 log yrs. This indicates a recent small burst of isolated star formation in the Eastern tail, small enough that only low mass clusters are present. Other similar bursts could have occurred in either tail between 7.0 and 8.0 log yrs, but would have faded from view by the present. It is clear, however that there is not continuous star formation at the level of that seen during the main interaction period, 8.0 - 8.8 log yrs ago.

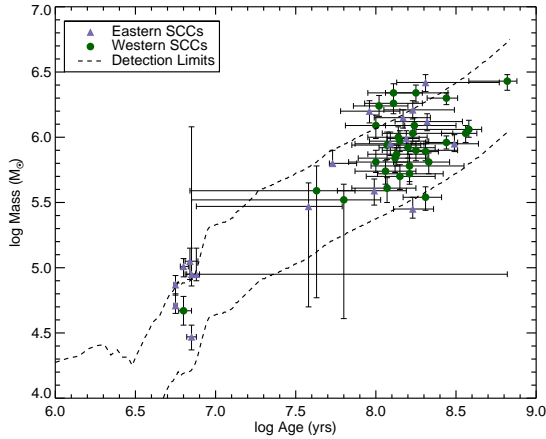


Figure 15. Ages and masses of SCCs for the Western (dark green) and Eastern (purple) tail. Dashed lines indicate our SCC detection threshold, as determined by our colour and magnitude limits. Two detection limits are formed from our upper and lower magnitude cuts. The gap between the young objects in the Eastern tail and the main distribution at ages of 8.0 - 8.8 log yrs shows we are seeing an isolated burst of star formation.

4.4 Spatial Distribution of SCCs and Diffuse Light

Spatial maps of tail colours and SCCs are shown in Figure 16 for both tails. Measurement boxes from Figures 5 are colour coded to indicate their $u-g$ colours. SCC positions and $u-g$ values are added in a similar manner.

The difference in age between the tails is evident in the abundance of younger regions, represented by cyan and yellow, in the Western tail, compared to older regions, represented by orange and red, in the Eastern tail. The spatial location of SCCs does not appear to influence the colour of the diffuse light. This is not too surprising, as these objects were masked out in Section 2.3.

Both of the tails show colour gradients across their lengths, with bluer colours near the galactic bulges and redder colours at the far tips. Likewise, the edges of the tails appear redder than their interiors. Such gradients were also seen among several tails in Mulia et al. (2015).

5 DISCUSSION

Distributions of $u-g$ colours for diffuse light and SCCs are shown in Figure 17. We can summarize Figure 17 with the following points:

- (i) The difference in $u-g$ colour between the Eastern and Western tail shows the total diffuse stellar light of the two tails are separated in age by over 500 Myr, with a significantly larger contribution from a young population in the Western tail.
- (ii) Assuming the two tails were formed at the same time, we find the stellar masses of the Eastern and Western tails to be dominated by old (~ 10 Gyr) populations drawn from the parent galaxies.
- (iii) While the Western tail contains a significant old (~ 10 Gyr) population, the stellar light is largely comprised of a

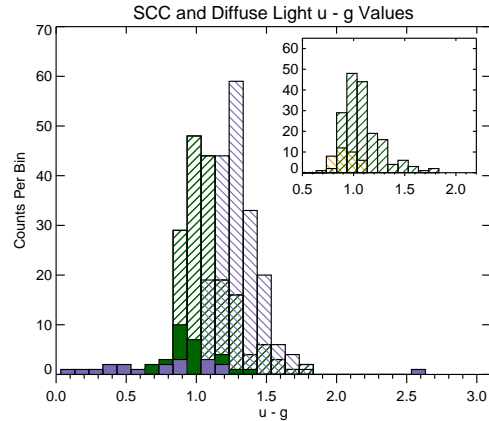


Figure 17. $u-g$ colour distribution for SCCs and diffuse light in NGC 3256W (dark green) and E (purple), with bin size of 0.1. Hashed histograms indicate diffuse light measurements, while solid histograms represent the SCCs Colour distributions for the separate diffuse structure in the Western tail are shown in the inset graph in orange, plotted alongside those of the Western tail itself (dark green). The diffuse light colours between the two tails are clearly distinct from one another. The distribution of SCC colour in the Western tail overlaps its diffuse light colour distribution, suggesting a common origin. SCCs in the Eastern tail are much younger than any of the SCCs in the Western tail.

population which formed soon after the interaction, with an age of 8.29 log yrs.

(iv) The similarity of the $u-g$ colour distribution of SCCs in the Western tail compared to the diffuse light gives credence to the idea that the Western tail is comprised of disrupted star clusters formed shortly after the formation of the tail, with the ones we see today being the ones that survived.

(v) The stark contrast in $u-g$ colours for SCCs in the Eastern tail as compared to the diffuse light colours suggests some very recent star formation as compared to the age of the tail.

Stellar populations in the two tails of NGC 3256 have different compositions. We base our conclusions on the assumption that the tails were formed at the same time. It's possible to interpret Figure 7 as due to the Eastern tail having formed first, with the stellar light we observe being formed from a burst of star formation caused by that earlier interaction. However, prograde collisions between galaxies are required to form tidal tails (D'Onghia et al. 2010; Toomre & Toomre 1972), as in the case of NGC 3256. In such a case, these tails form simultaneously, which indicates a common age between NGC 3256's tails. Lıpari et al. (2000) found three nuclei within the centre of NGC 3256, leading them to construct a merger scenario involving two separate mergers and three galaxies. The Eastern tail could be explained to have formed during the first merger, while the Western tail formed later with a prograde interaction between the merger remnant and the third galaxy. However, Lıpari et al. (2000) suggests a more likely scenario with the two major galaxies initially merging, and a smaller satellite galaxy merging after the major interaction, supported in further work by Lıpari et al. (2004). Additionally, English et al. (2003) only observed two broad H I tails, leading them to conclude that

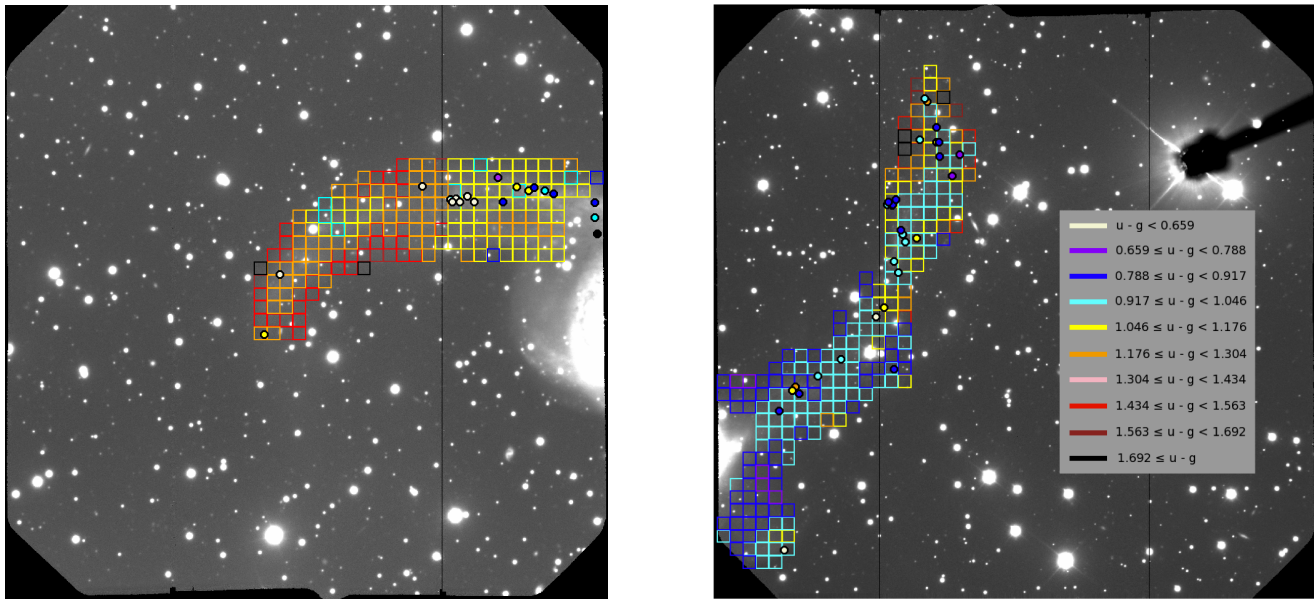


Figure 16. *Left:* Spatial distribution of diffuse light and SCC $u-g$ colours for the Eastern tail. *Right:* Same, but for the Western tail. Colour code is reproduced from Figure 12. Each tail shows a gradient in colour across their length, suggesting a decrease in the fraction of young stars within the diffuse light along the tail from centre to tip.

NGC 3256 is likely created by a two galaxy prograde merger. Given these works, it is very probable that the two tails were formed at the same time. We also find possible evidence for the small satellite merger in the separate diffuse structure, seen in the Western tail. This structure is younger than either tail, supporting the theory of a late minor merger, occurring after the major merger.

The diffuse light in the Western tail is dominated by a younger population, formed soon after the formation of the tail. This population is also present in the Eastern tail, although at a lower concentration. The source of the young population is uncertain, as stars may form in a variety of methods: in bound clusters, unbound stellar associations, down to near individual stellar formation. The fraction of stars forming in clusters can be up to 70% in regions of large gas density (Kruijssen 2012). However, these clusters are subject to frequent tidal shocks which will preferentially destroy low mass clusters (Kruijssen et al. 2012), dispersing their material into the diffuse tidal light and making clusters an ideal candidate for the source of our young population. The destruction of star clusters is modeled in two parts: number loss (removal of stars in a cluster) and mass loss (removal of mass in a cluster). Number loss can be understood as effects from stellar feedback, such as stellar winds and supernovae, which expel gas in a cluster, causing it to become unbound. Mass loss will remove stars from a cluster via two-body interactions. Number loss, also known as infant mortality, will only be important for the first ~ 10 Myr, as the hot and massive stars evolve and explode. The remnants of these clusters are thus seen as the diffuse light of the tail. A similar effect is seen in NGC 7714 – ages of HII regions within the tidal tails have been shown to be older than star clusters residing within them, suggesting previously formed clusters have been dispersed and surround the newly conceived clusters (Peterson et al. 2009). The coincidence of peaks in histograms of $u-g$ colour between the diffuse light

of the Western tail and its SCCs (Figure 17) strongly suggests the two are intertwined. Results of KS tests show the populations are distinct from each other, however, this is likely due to the presence of an old stellar population in the diffuse light of the tail. The timescale between tail formation and cluster formation is separated by ~ 200 Myr. We compare this to simulations of NGC 4038/9, a similar merger, which found a peak in star formation ~ 25 Myr after the interaction (Renaud et al. 2015).

Individual masses of SCCs in the Western tail are on average more massive than in the Eastern tail, as shown in Figure 15, although the Eastern tail has several very young, low mass objects absent in the Western tail. The greater number of SCCs for the Western tail can be attributed to its larger HI mass. This can be related back to the diffuse light as well, as the Western tail’s higher abundance of gas led it to form more star clusters which could be disrupted and dispersed in the tail. We compare the ages of our clusters to those found in the nuclei from previous studies. Trancho et al. (2007) spectroscopically studied 23 star clusters inside the centres of the galaxies, finding an average age of ~ 10 Myr. Zepf et al. (1999) performed photometry on several hundred objects within the centre finding bright and blue objects. Our SCCs are substantially older than those found within the nuclei, suggesting the star formation in the tails was cut off earlier relative to the interior. This is consistent with spectroscopic observations of star clusters in the Western tail by Trancho et al. (2007) and photometric analysis of SCCs in the Eastern tail by Mulia et al. (2015), both of whom found ages of clusters to be older than those in the interior. A similar viewpoint is shared in the Antennae simulations, which show a cessation of star formation in the tails, while star formation in the interiors is ongoing (Renaud et al. 2015). Star formation in the interiors can be stimulated as material previously thrown out during the initial encounters falls back into the centre of the potential well.

Of particular interest are the very young objects found in the Eastern tails, with $u-g < 0.7$. These objects indicate relatively recent star formation in a tail whose diffuse light suggests a limited star formation history. It is possible these objects are now being formed as material falls back through the tail to the interiors, creating turbulence in the H I gas and sparking small bursts of star formation. We do not see these very young objects in the Western tail. However, note that they are low mass, with masses $< 10^5 M_{\odot}$. They will fade from detectability as they age (see Figure 15); additionally, they may be subject to tidal shocks from regions of dense gas which can disrupt them. This suggests that there may be small star formation events periodically in both tails, but the evidence of these events will rapidly fade away.

Mullan et al. (2013) found that tidal tails with large H I line of sight velocity dispersion σ_{los} and high H I column densities were ideal locations for SCCs. Both the 3256 tails fit these criteria, and the majority of their SCCs, as determined by Knierman et al. (2003) using *HST* WFPC2 data, lie in H I pixels with these characteristics. However, the tails can be distinguished by measurements of shear ($d v_{\text{los}}/d r_{\perp}$), with the Western tail's shear about one-third that of the Eastern's. Mullan et al. (2013) found that SCCs were preferentially located in regions of low shear, which is suggestive that these areas can be ideal for star formation. We reproduce spatial maps of H I shear from Figures 4.18 and 4.19 in Mullan et al. (2013), and compare them to our spatial $u-g$ maps in Figure 18 for the Eastern tail and Figure 19 for the Western tail.

From Figure 18, two pockets of low shear are visible in yellow. The first of these, closest to the bulge, corresponds to the location of the youngest SCCs in the Eastern tail, visualized as beige circles. The second low shear region does not contain any SCCs, although the diffuse light near this area is younger than its surroundings.

The Western tail has a ridge of low shear seen in Figure 19, running from the middle of the tail to the tip. We find the majority of SCCs within the H I field of view reside in this region, with few (~ 3 out of 23) outside. The diffuse light appears to follow the shear as well. At the tip of the tail, the low H I shear seen in blue matches the yellow diffuse light boxes. As the shear increases to yellow and orange, the diffuse light reddens and the boxes shift to orange and red.

The effect of dust on the diffuse light in these tails is similar to that of an older population; in either case the colours are reddened. To investigate this effect, we redden the Eastern tail colour to match the Western's, by minimizing the distance between the two values. We find the amount of extinction needed for this is $A_V \approx 0.6$, which we find unrealistic, as tidal tails are regions of relatively low extinction (Tran et al. 2003; Bastian et al. 2005). Additionally, examination of archival *GALEX* NUV data (Gil de Paz et al. 2007) show similar brightnesses for the two tails, suggesting similar levels of low extinction. Extinction in the Eastern tail would dim the *GALEX* data, with respect to the Western tail, but this is not seen. Mulia et al. (2015) examined the $B-V$ colour distribution within the Eastern tail, finding negligible levels of reddening, supporting the lack of dust within the tails.

We finally look at extinction in the three star clusters spectroscopically studied in the Western tail from Trancho et al. 2007, which are listed at 0.0, 0.3, 0.5 A_V mag, showing

minimal extinction. Additionally, as mentioned in Section 4.3.2, several of our young SCCs are subject to internal extinction. Extinction values of these objects range from 1.1 to 0.7 A_V mag. Dust can be expected to associate with star clusters, as dust is needed for star formation, so we expect to see the most extinction in these regions. However, such levels of extinction exist for a small handful of objects, and as these are masked and do not factor into our LSB measurements, we are led to believe extinction does not significantly affect our analysis of the stellar age and mass distribution.

6 CONCLUSION

Our observational program has proven successful in allowing us to characterize the stellar populations of our tidal tails. We find NGC 3256W to be bluer than its twin tail, NGC 3256E. Measured colours indicate that diffuse light in the Western tail has a large contribution from a young population formed after the interaction, perhaps from dispersed star clusters, as compared to the Eastern tail, which is primarily illuminated by an old population derived from the host galaxy. Both tails exhibit colour gradients along their lengths, suggesting a gradient in the time scale of star formation. Despite these colour differences, both tails appear to be dominated in mass by an old, underlying population, originating from the interacting galaxies.

Analysis of SCCs shows a lack of old objects in either tail ($> 10^9$ yr), but a clustering of objects below 400 Myr in the Western tail and Eastern tail. The Eastern tail shows an interesting clustering of young objects, with ages $< 10^7$ yr. These objects are low mass structures and are not likely to be detected as they age, disappearing as they fade beyond our detection limits, or are dispersed into the tail. The $u-g$ colour distribution of the Western SCCs is proven to be distinct from the diffuse stellar light in the Western tail through KS probability tests, however the peaks of the colour distributions of the diffuse light and SCCs match well, suggesting these objects and regions are intertwined. The fact that the KS test shows separate populations can be explained by the addition of an old, underlying stellar population to the diffuse light.

NGC 3256 has been shown in past studies to contain a large number of SCCs compared to other systems (Mullan et al. 2011; Knierman et al. 2003). We plan to apply our current observational program to additional tidal tail systems with varying amounts of SCCs and H I properties, particularly those with low numbers of SCCs. The presence of a tidal dwarf galaxy may also play a role in determining the composition of tidal tail diffuse light. *GALEX* observations of the Antennae galaxy reveal a gradient in colour along the tail, with bluer colours near the tip of the Southern tail, where two tidal dwarf galaxies reside (Hibbard et al. 2005). Knierman et al. (2003) found that tails with tidal dwarfs did not contain as many SCCs as those without them. Have these structures already dispersed their clusters into their tails, or has there been a complete absence of star cluster formation? This remains to be seen.

We would like to thank the anonymous referee for helpful comments which have improved the quality and content of this paper. Based on observations obtained at the Gemini Observatory (program ID GS-2013A-Q-57, processed using

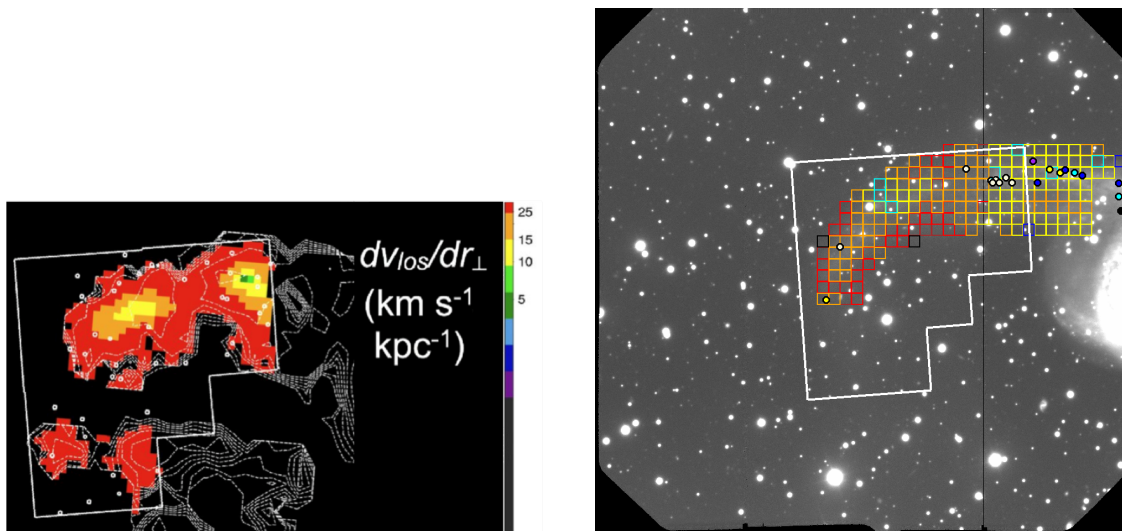


Figure 18. *Left:* HI shear measurements for the Eastern tail (Mullan et al. 2013). The WFPC2 footprint is overlaid in solid white. Dashed white contour lines correspond to $\log N_{\text{HI}} = 20.0 - 21.4 \text{ cm}^{-2}$ in steps of 0.2 dex, while white circles are SCCs as determined by Knierman et al. (2003). *Right:* $u-g$ spatial map of the Eastern tail, with the WFPC2 footprint overlaid in white. Two regions of relatively low shear can be seen (yellow and orange regions in the left-hand panel), one at the edge of the WFPC2 footprint near the bulge, the other in the centre. The first can be matched in our $u-g$ spatial distribution to the group of young SCCs mentioned in the previous paragraph. The second corresponds to a patch of yellow boxes of diffuse light (right-hand panel).

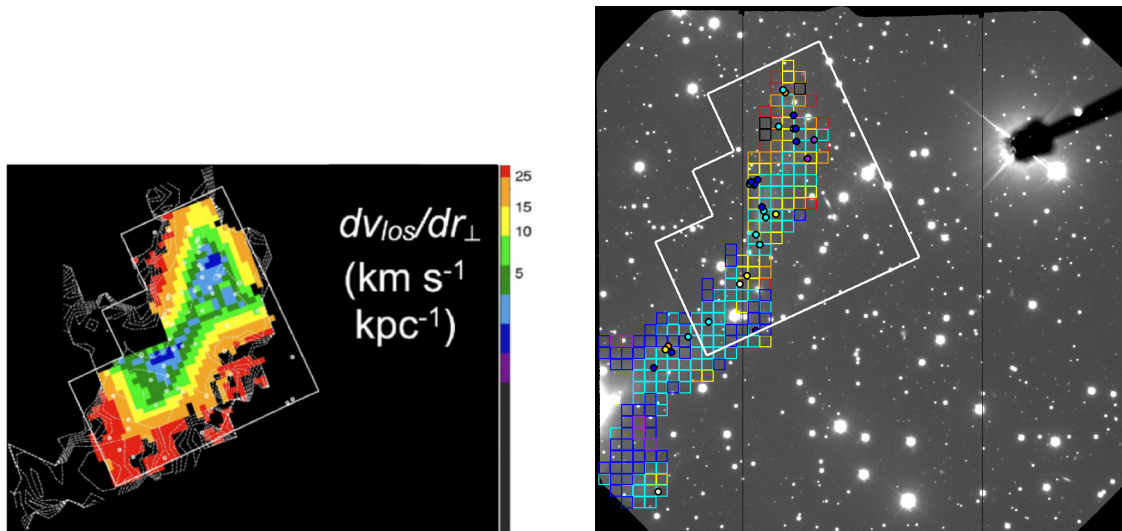


Figure 19. Same as Figure 18, but for the Western tail. The majority of detected SCCs within the WFPC2 footprint lie in the spine of low shear (green and blue in the left-hand panel), with measurements less than 5 km/s/kpc .

the Gemini IRAF package), which is operated by the Association of Universities for Research in Astronomy, Inc., under a cooperative agreement with the NSF on behalf of the Gemini partnership: the National Science Foundation (United States), the National Research Council (Canada), CONICYT (Chile), Ministerio de Ciencia, Tecnología e Innovación Productiva (Argentina), and Ministério da Ciência, Tecnologia e Inovação (Brazil). The Digitized Sky Surveys were produced at the Space Telescope Science Institute under U.S. Government grant NAG W-2166. The images of these surveys are based on photographic data obtained using the Oschin Schmidt Telescope on Palomar Mountain and the UK Schmidt Telescope. The plates were processed

into the present compressed digital form with the permission of these institutions. SCG thanks the Natural Science and Engineering Research Council of Canada for support. KK is supported by an NSF Astronomy and Astrophysics Postdoctoral Fellowship under award AST-1501294. The Institute for Gravitation and the Cosmos is supported by the Eberly College of Science and the Office of the Senior Vice President for Research at the Pennsylvania State University.

REFERENCES

- Bastian, N., Hempel, M., Kissler-Patig, M., Homeier, N. L., & Trancho, G. 2005, *A&A*, 435, 65
- Bastian, N., Trancho, G., Konstantopoulos, I. S., & Miller, B. W. 2009, *ApJ*, 701, 607
- Bik, A., Lamers, H. J. G. L. M., Bastian, N., Panagia, N., & Romaniello, M. 2003, *A&A*, 397, 473
- Chabrier, G. 2001, *ApJ*, 554, 1274
- de Mello, D. F., Mendes de Oliveira, C., Torres-Flores, S., & Urrutia-Viscarra, F. 2011, *Revista Mexicana de Astronomia y Astrofisica Conference Series*, 40, 54
- D’Onghia, E., Vogelsberger, M., Faucher-Giguere, C.-A., & Hernquist, L. 2010, *ApJ*, 725, 353
- English, J., Norris, R. P., Freeman, K. C., & Booth, R. S. 2003, *AJ*, 125, 1134
- Hibbard, J. E., Rupen, M., & van Gorkom, J. H. 2001, *Gas and Galaxy Evolution*, 240,
- Hibbard, J. E., Bianchi, L., Thilker, D. A., et al. 2005, *ApJL*, 619, L87
- Fedotov, K., Gallagher, S. C., Konstantopoulos, I. S., et al. 2011, *AJ*, 142, 42
- Gallagher, S. C., Durrell, P. R., Elmegreen, D. M., et al. 2010, *AJ*, 139, 545
- Gil de Paz, A., Boissier, S., Madore, B. F., et al. 2007, *ApJS*, 173, 185
- Knierman, K. A., Gallagher, S. C., Charlton, J. C., et al. 2003, *AJ*, 126, 1227
- Konstantopoulos, I. S., Gallagher, S. C., Fedotov, K., et al. 2012, *ApJ*, 745, 30
- Kroupa, P. 2001, *MNRAS*, 322, 231
- Kruijssen, J. M. D., Pelupessy, F. I., Lamers, H. J. G. L. M., Portegies Zwart, S. F., & Icke, V. 2011, *MNRAS*, 414, 1339
- Kruijssen, J. M. D. 2012, *MNRAS*, 426, 3008
- Kruijssen, J. M. D., Pelupessy, F. I., Lamers, H. J. G. L. M., et al. 2012, *MNRAS*, 421, 1927
- Leitherer, C., Schaerer, D., Goldader, J. D., et al. 1999, *ApJS*, 123, 3
- Lipari, S., Díaz, R., Taniguchi, Y., et al. 2000, *AJ*, 120, 645
- Lipari, S. L., Díaz, R. J., Forte, J. C., et al. 2004, *MNRAS*, 354, L1
- Marigo, P., Girardi, L., Bressan, A., et al. 2008, *A&A*, 482, 883
- Mulia, A. J., Chandar, R., & Whitmore, B. C. 2015, *ApJ*, 805, 99
- Mullan, B., Konstantopoulos, I. S., Kepley, A. A., et al. 2011, *ApJ*, 731, 93
- Mullan, B., Kepley, A. A., Maybhate, A., et al. 2013, *ApJ*, 768, 194
- Peterson, B. W., Struck, C., Smith, B. J., & Hancock, M. 2009, *MNRAS*, 400, 1208
- Renaud, F., Bournaud, F., Kraljic, K., & Duc, P.-A. 2014, *MNRAS*, 442, L33
- Renaud, F., Bournaud, F., & Duc, P.-A. 2015, *MNRAS*, 446, 2038
- Renaud, F., Boily, C. M., Naab, T., & Theis, C. 2009, *ApJ*, 706, 67
- Salpeter, E. E. 1955, *ApJ*, 121, 161
- Salzer, J. J., Jangren, A., Gronwall, C., et al. 2005, *AJ*, 130, 2584
- Schombert, J. M., Wallin, J. F., & Struck-Marcell, C. 1990, *AJ*, 99, 497
- Schlafly, E. F., & Finkbeiner, D. P. 2011, *ApJ*, 737, 103
- Schweizer, F. 1987, *Nearly Normal Galaxies. From the Planck Time to the Present*, 18
- Schweizer, F. 1978, *Structure and Properties of Nearby Galaxies*, 77, 279
- Smith, J. A., Tucker, D. L., Kent, S., et al. 2002, *AJ*, 123, 2121
- Toomre, A., & Toomre, J. 1972, *ApJ*, 178, 623
- Torres-Flores, S., de Oliveira, C. M., de Mello, D. F., Scarano, S., & Urrutia-Viscarra, F. 2012, *MNRAS*, 421, 3612
- Tran, H. D., Sirianni, M., Ford, H. C., et al. 2003, *ApJ*, 585, 750
- Trancho, G., Bastian, N., Schweizer, F., & Miller, B. W. 2007, *ApJ*, 658, 993
- Trancho, G., Bastian, N., Miller, B. W., & Schweizer, F. 2007, *ApJ*, 664, 284
- Zepf, S. E., Ashman, K. M., English, J., Freeman, K. C., & Sharples, R. M. 1999, *AJ*, 118, 752

This paper has been typeset from a \TeX / \LaTeX file prepared by the author.